High-temperature and abrasion-resistant metal-insulator-metal metamaterials

Y. Tian [a], L. Qian [b], X. Liu [a], A. Ghanekar [c], J. Liu [d, e], T. Thundat [f], G. Xiao [b], Y. Zheng [a, *]

[a] Department of Mechanical and Industrial Engineering, Northeastern University, Boston, MA, 02115, USA
[b] Department of Physics, Brown University, Providence, RI, 02912, USA
[c] Ming Hsieh Department of Electrical and Computer Engineering, University of Southern California, Los Angeles, CA, 90089, USA
[d] Department of Mechanical and Aerospace Engineering, University at Buffalo, The State University of New York, Buffalo, NY, 14260, USA
[e] RENEW Institute, University at Buffalo, The State University of New York, Buffalo, NY, 14260, USA
[f] Department of Chemical and Biological Engineering, University at Buffalo, The State University of New York, Buffalo, NY, 14260, USA

ARTICLE INFO

ABSTRACT

Selective solar absorbers (SSAs) with high performance are the key to concentrated solar power systems. Optical metamaterials are emerging as a promising strategy to enhance selective photon absorption, however, the high-temperature stability (>500 °C) remains as one of the main challenges for practical applications. Here, a multilayered metamaterial system (Al_2O_3/W/SiO_2/W) based on metal-insulator-metal Fabry-Pérot resonance effect has been demonstrated with high solar absorptance over 92%, low thermal emittance loss below 6% (100 °C blackbody), and significant high-temperature thermal stability: it has been proved that the optical performance remains 94% after 1-h thermal annealing under ambient environment up to 500 °C, and 94% after 96-h thermal cycle test at 400 °C. Outdoor tests demonstrate that a peak temperature rise (193.5 °C) can be achieved with unconcentrated solar irradiance and surface abrasion resistance test yields that SSAs have a robust resistance to abrasion attack for engineering applications.

© 2021 Elsevier Ltd. All rights reserved.

1. Introduction

Solar energy is abundant, striking our earth at a rate of 90,000 TW, which is 5000 times of our current global power consumption [1]. The conversion of solar energy is considered as a promising approach to address the energy and environmental crisis. To date, various solar energy conversion technologies have been developed including photovoltaics [2], photo-thermal methods [3], and artificial photosynthesis [4]. Among those technologies, solar thermal power systems, such as concentrated solar power (CSP) via Rankine cycle [5], solar thermoelectric generators [6], and solar thermophotovoltaics [7] have attracted increasing attention recently for various environmentally sustainable applications in industrial heating [8], air conditioning [9], and electricity generation [6]. As a crucial element, selective solar absorbers (SSAs), which are capable of converting solar radiation into heat, have a considerable influence on the overall performance of solar thermal systems. However, it is challenging to achieve high thermal stability of the SSAs, which operates under a sever high-temperature working environment. Therefore, it is crucial to boost the performance of solar thermal systems by enhancing the sunlight absorption capability by depositing the infrared anti-reflection layer [10] and improved the stability under high-temperature environment [11]. Furthermore, SSAs are required to be omnidirectional and polarization-insensitive in the solar irradiance regime due to the randomly distributed solar irradiation [12]. Additionally, the cutoff wavelength of a selective absorber, at which its absorptance spectrum changes steeply, is highly dependent on its operational temperature because of the shifting nature of blackbody radiation according to Wien's displacement law [13]. However, existing technologies are either relied on high-cost nanofabrication methods or suffer from poor thermal stability in the ambient environment [14] and the omnidirectional and polarization insensitivity are scarcely achieved. Hence, SSAs with high-temperature ambient stability and omnidirectional and polarization insensitivity are highly demanded in solar thermal applications.

* Corresponding author.
E-mail address: y.zheng@northeastern.edu (Y. Zheng).

Recently, advances in the small-scale fabrications have enabled the manipulation of sunlight trapping in micro/nanostructures. Excitation of plasmonic and Fabry-Pérot (FP) resonance can produce selective and tunable absorption peaks at different wavelengths [15-18]. Simultaneously, the alternation from high UV/visible absorptance to low mid-infrared emittance is sharp as compared with natural material-–based SSAs. Abundant metamaterial-based selective absorbers have been investigated, such as 1D or 2D surface gratings [19,20], nanoparticles embedded dielectrics [21], crossbar or nanodisk arrays [22], and photonic crystals [23]. Nevertheless, these absorbers depend on time-consuming nanofabrication technologies, such as photolithography and electron beam lithography, which makes them unrealistic to be scalable-manufactured. Moreover, the high temperature will yield permanent damage to SSAs' spectral selectivity.

Metal-insulator-metal (MIM)–based solar absorbers [24,25] consist of two metallic layers with a thin dielectric layer sandwiched in between. In an FP resonator, two metal layers are separated by a lossless dielectric spacer and the reflectance and transmittance can be controlled by changing the thickness of the dielectric spacer to manipulate the incident and reflected light. The FP resonance shows a broadband absorption that is desired for SSA applications. It provides a high absorptance at the solar wavelengths, while the bottom layer is thick enough to possess a high reflectivity in the thermal infrared region to depress the spontaneous blackbody thermal radiation. Some ceramic materials such as Al_2O_3, SiO_2, AlN, and TiN can be deposited on the top metal layer of MIM nanostructures to prevent the oxidation of metal at a high temperature. MIM-based absorber is feasible to be scale-manufactured with vacuum deposition methods like sputtering [26], evaporation [27] or chemical vapor deposition [28]. Although high wavelength selectivity has been demonstrated on the multilayer-based SSAs structures, their high-temperature stability is far from satisfying, mainly due to the lack of materials optimization. The refractory metals or metal oxides, including tungsten (W) [29], nickel (Ni) [30], chromium (Cr) [26], silica (SiO_2) [31], alumina (Al_2O_3) [32], and chromia (Cr_2O_3) [33] have been applied to manufacture SSAs. Specifically, W, Ni, and Cr thin film display high reflectivity in the mid-infrared wavelength region [19], while maintaining the high absorptance in solar wavelength when they are in the form of nanoparticles [34]. On the other hand, oxides such as SiO_2, Al_2O_3, and Cr_2O_3 have high-temperature stability even in the ambient environment. Here, we report a MIM-based (W–SiO_2–W) SSAs that show high spectral selectivity (solar absorptance/thermal emittance = 13.9) and high thermal efficiency (80.03% without optical concentration, compared to the state of the art 78% [12]). The spectral selectivity of fabricated SSAs is angular-independent (up to 75° compared to the state of the art up to 60° [35]) and polarization-insensitive (0° or 90°). The optical performance remains 93.6% and 94.1% after 1-h thermal annealing up to 500 °C and 96-h thermal treatment cycle at 400 °C, respectively. Compared with other fabrication methods, such as plasma-enhanced chemical vapor deposition, e-beam lithography, and reactive-ion etching, magnetron sputter is more feasible to be applied into industrial fabrication, while the fabricated MIM solar absorber exhibits better thermal stability than those cermet-based solar absorbers manufactured by electroplating, anodization, and evaporation (Table S1) [12,36-38]. Even though some commercial products, e.g., TiNOX and SOLKOTE [39,40], show high spectral selectivity for a targeted working temperature of 100 °C, our designed structures have the flexibility to optimize its structural parameters, such as materials and thickness of different layers, to fit the applications of various targeted temperatures for both concentrated and unconcentrated solar thermal engineering. A high stagnation temperature of 193.5 °C was achieved under unconcentrated solar irradiance, which indicates its wide feasibility of low-temperature solar thermal applications without a solar concentrator. The sandpaper abrasion robustness tests are also conducted in this work to demonstrate the mechanical abrasion resistance of SSAs' surface.

2. Materials and methods

2.1. Materials

SiO_2 (99.995%, 4N5), Al_2O_3 (99.995%, 4N5), and W (99.995%, 3N5) are purchased from Angstrom Sciences, Inc. 2 inches wafers (Type: P; dopant: B; orientation: < 1−0−0 >; resistivity: 10−20 Ω/cm; thickness: 279 ± 25 μm) are purchased from WaferPro.

2.2. Methods

2.2.1. Sample fabrication and SEM topography characterizations

SSAs samples are deposited with a magnetron sputtering technique using a home-built high-vacuum sputtering system (Supporting Fig. S1). The fabrication process has been described in detail in this publication [41]. The fabrication parameters, such as deposition rate, base pressure, and sputtering power for each deposition procedure are specified in Table S2. The base pressure before sputtering is 3.4×10^{-7} Torr. The Al_2O_3 and W layer are both deposited directly from Al_2O_3 and W target, respectively, while the SiO_2 layer is oxidized from the silicon (Si) with radio frequency (RF) sputtering. The cross-section and topography of absorber samples after various temperature thermal annealing and diverse long-time thermal stability tests are characterized by SIGMA VP field emission-scanning electron microscope (FE-SEM).

2.2.2. Optical properties measurements

Hemispherical reflectance measurements in the UV, visible, and near-infrared regions (0.3 μm − 2.5 μm) are performed on a Jasco V770 spectrophotometer with a 60 mm polytetrafluoroethylene (PTFE)-based integrating sphere. A wavelength scan step is fixed as 1 nm with angles of incident (AOI) of 6° and normalized to a labsphere spectralon reflectance standard. The mid-infrared (2.5 μm − 15 μm) reflectance measurements are executed on Jasco 6600 FTIR spectrometer together with a Pike 3-inches golden integrating sphere. The AOI of the incident beam from the FTIR spectrometer is fixed at 12° and the diffused golden reference is selected as a normalized standard. These spectra are taken at a scan rate of 64 with a wavelength resolution of 0.4 cm^{-1}. The hemispherical reflectance measurement for different AOI is conducted by using home-built wedge blocks (Supporting Fig. S2, 18°, 30°, 33°, 33°, 51°, 66°, and 76°) combined with the Jasco 60 mm PTFE-based integrating sphere and Pike 3-inches golden integrating sphere. The wedge blocks for PTFE integrating sphere are put faced to the sample ports of the Jasco and Pike integrating sphere. SSAs samples and the reference standard are located at the sample ports on these designed wedge blocks. The background spectrum and the reflectance spectrum are taken as usual to get the reflectivity spectra. The specular reflectance measurements of variable angle in the UV, visible, and near-infrared regions (0.3 μm − 2.5 μm) are performed on Jasco V770 spectrophotometer with Harrick variable angle reflection accessory. The variable angle specular reflectance measurements (2.5 μm − 15 μm) are executed on Jasco 6600 FTIR spectrometer together with the Harrick Seagull^{TM} Variable Angle Reflection Accessory. Both measurements are taken for angles of 12°, 30°, 45°, 60°, and 75°. The hemispherical reflectance measurements of variable polarization angle from 0.3 μm to 2.5 μm are done on the Jasco V770 spectrophotometer with GPH-506 polarizer and 60 mm integrating sphere. The hemispherical reflectance

measurements of variable angle polarization from 2.5 μm to 15 μm are executed on Jasco 6600 FTIR spectrometer together with PL-82 polarizer and Pike 3-inches golden integrating sphere.

2.2.3. High-temperature thermal annealing and stability tests

High-temperature thermal annealing and stability tests are both carried out in a tube oven at an ambient atmosphere with an alumina tube of 5 cm diameter and 80 cm length. Samples are put in an alumina crucible boat (100 mm × 30 mm × 20 mm) that is placed in the center of the tube. The increasing rate of temperature is set to be at 15 °C/min for 100 °C, 200 °C, 300 °C, 400 °C, and 500 °C for 1 h. The hemispherical reflectance measurements are carried out after each thermal treatment. For the high-temperature thermal stability tests, the temperature controller of the tube oven is set to be 400 °C for 12 h, 24 h, 48 h, 72 h, and 96 h thermal cycles. The samples are taken out after each thermal cycle for reflectance spectrum measurement and a small piece of the sample (~ 3 mm × 3 mm) is cut for SEM topography characterization.

2.2.4. Real-time reflectivity measurement of SSAs under high vacuum

The real-time measurement of reflectivity for SSAs is conducted on Jasco FTIR 6600 spectrometer within the Harrick high-temperature reaction chamber. The chamber can be heated by an electrical heater up to 910 °C and vacuumed down to <10^{-3} Pa connected to a Pfeiffer TMH 260 turbo pump. The temperature of the SSAs is measured by a K-type thermocouple and controlled by the Waterloo PID temperature controller.

2.2.5. SSAs' surface abrasion robustness tests

A sandpaper abrasion test is carried out using a 400 grit SiC sandpaper as an abrasion surface (Supporting Fig. S3). The SSAs samples with a weight of 50 g/100 g above it are put facedown to sandpaper and move 10 cm along the ruler (Supporting Fig. S3b). Then, the sample is rotated counterclockwise by 90° (face to the sandpaper) and move 10 cm along the ruler. The three steps shown in Supporting Fig. S3b are defined as one abrasion cycle. This guarantees that the SSAs' surface is abraded longitudinally and transversely in each cycle. The reflectivity spectra are measured after 1, 3, 5, 10, 20, 30, and 50 cycles.

3. Results and discussion

3.1. Energy conversion efficiency analysis of the SSAs

According to the Planck's formula of blackbody radiation intensity distribution, we know that the solar intensity and the blackbody intensity for mid-temperatures (300 °C ~ 500 °C) are distributed over different wavelength regimes (Fig. 1a). The spectral irradiance of a 400 °C blackbody is at the same order of solar heat flux, while it will be twice as the solar intensity when the temperature of blackbody increases to 500 °C. Meanwhile, the expanded regime of blackbody radiation moves to a shorter wavelength as its temperature increases, as illustrated by peaks of the blackbody irradiance curves from 100 °C to 500 °C (Fig. 1a). The solar absorber is a key component to transfer the solar energy into heat in solar thermal engineering systems. When it is heated up, it radiates heat as infrared thermal radiation. The thermal loss due to the thermal re-emission depresses the solar-to-heat efficiency of the solar thermal system. Therefore, an ideal spectral selective absorber has a unity absorptance in the solar radiation regime and a zero emittance in the thermal-infrared region to depress the thermal re-emission from the blackbody, with a sharp transition between these two regions. The cutoff wavelength, $\lambda_{cut-off}$, at which the transition happens, is where the blackbody radiation begins to

exceed the solar intensity. The ideal transition wavelength ($\lambda_{cut-off,ideal}$) will shift to shorter wavelengths, called blue-shift, for a higher operational temperature when the concentration factor (CF) is fixed. $\lambda_{cut-off,ideal}$ will shift to longer wavelength, called red-shift, for a higher CF when the operational temperature is fixed. Consequently, it is a trade-off to design perfect SSAs at different engineering applications. The efficiency of SSAs, η_{abs}, can be simplified as: $\eta_{abs} = \alpha_{abs} - \varepsilon_{abs}\left[\sigma\left(T_{abs}^4 - T_{amb}^4\right)\right]\Big/(CF \cdot Q_{abs})$, where α_{abs} and ε_{abs} stand for the solar absorptivity and thermal emissivity of SSAs, respectively, and σ is the Stefan-Boltzmann constant. T_{abs} and T_{amb} are the operational temperatures of the solar absorber and the environment, respectively. CF represents the area ratio of the solar collector aperture area and the solar absorber area, and Q_{abs} is the solar radiative heat flux at AM 1.5 (global tilt). Fig. 1b and c are the 3D contour plots which illustrate the energy conversion efficiency, η_{abs}, as a function of the cutoff wavelength and the CF at different operational temperature, T_{abs}, of 500 °C, and 800 °C, in which the red color represents higher efficiency, while the blue means lower efficiency (plots by analyzing formulas section 1 in Supplementary material). The efficiency curves share the same trend of increasing to a maximum from 0 and then decrease as $\lambda_{cut-off}$ sweeps from 0.25 μm to 4.0 μm (Fig. 1b and c). The maximum efficiency of the 500 °C SSAs (Fig. 1b), increases with the CF varying from 1 to 100 at a fixed cut-off wavelength, which can be seen that the red color is getting deeper. The efficiency, η_{abs}, will increase when the CF increases since it is in the denominator. Additionally, the corresponding cut-off wavelength will shift to a longer wavelength with the increasing of CF, since the red-shift ensures that the SSAs absorb more solar energy. By comparing Fig. 1b and c, it shows that the maximum energy efficiency of the same corresponding CF drops with the increasing of operational temperature (black points in Fig. 1b and c). It is reasonable that the energy efficiency, η_{abs}, decreases with the increasing of absorber operational temperature, T_{abs}, because T_{abs} is in the numerator. When the materials of the MIM-based SSAs are chosen, the cutoff wavelength can be shifted by changing the thicknesses of the different layers. The materials of various layers are chosen as Al_2O_3, W, SiO_2, and W from the top to bottom. Their optimized thicknesses of this four-layer stack are obtained by tuning their respective variables to reduce the discrepancy between the calculated spectra and the spectra of a desired ideal SSA. This process involves an optimization procedure that aims to minimize the error between the calculated and desired spectra. The error between these two spectra is given by $\delta = \sum_{i=1}^{n}[r_c - r_i]^2$. Here, r_c and r_i are calculated and desired reflectivity spectra of the solar absorbers. Index i refers to the ith wavelength (0.3 μm − 20 μm) over which the computational analyses are conducted.

3.2. Characterizations of sample radiative properties

Fig. 1d illustrates the 3D schematic of a proposed multilayered stack consisting of five layers. Fig. 1e manifests that the fabricated SSA is black at various angles with visual observation, which elucidates its high absorptance in the visible wavelength. The hemispherical reflectivity which exhibits spectral selectivity with solar reflectivity $R_{abs} < 0.06$ in the solar spectrum and thermal reflectively $R_{abs} > 0.94$ in the mid-infrared region. The thickness of different layers for the fabricated sample is confirmed by the cross-section view of FE-SEM shown in Fig.1f. The bottom W layer is thick enough to block all the incident light and the solar absorptance of the absorber, $\alpha = 1 - R_{abs}$. Fig. 1g shows the hemispherical reflectivity spectra of the fabricated MIM solar absorber which exhibits an overall solar absorptance of 0.92 and thermal emittance of 0.06. The high solar reflectance results from the strong FP resonance in
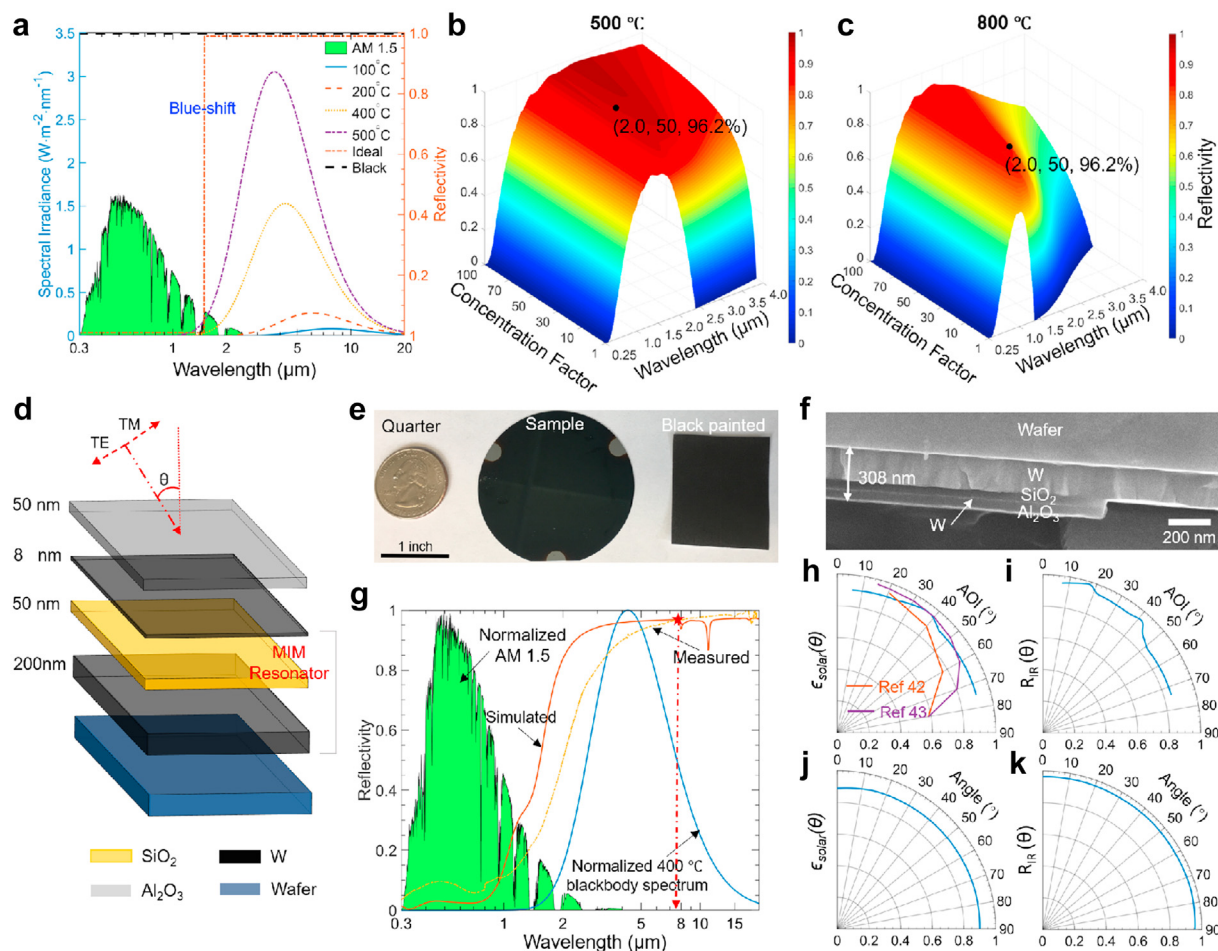
Fig. 1. (a) Solar spectral irradiance (AM 1.5, global tilt), radiative heat flux of blackbody thermal radiation at various temperatures, and reflectivity spectra of ideal SSAs and black surfaces. (b) and (c) The 3D plot of solar to heat energy conversion efficiency for SSAs' contour plotted against concentration factor (CF) and cutoff wavelength at different operational temperatures of 500 °C and 800 °C, respectively. (d) 3D schematic of proposed multilayer stack consisting of W, Al$_2$O$_3$, and SiO$_2$. The incidence angle, θ, is defined as the angle between solar incident radiation and the normal direction of the surface. (e) A photo of sample fabricated on a 2-inch silicon wafer compared with a quarter coin (24 mm in diameter) and black painted paper (3 cm × 3 cm). (f) A cross-section SEM micrograph of the fabricated sample, the 2D schematic shows the thickness of each layer for the multilayer stack. (g) Normalized spectral distribution for the radiative heat flux of solar (ASTM G173 AM 1.5) and blackbody thermal radiation (400 °C), as well as simulated and measured reflectivity spectra of multilayer solar absorber. (h) The SSAs' high absorptance ε_{solar} (θ) (0.3 μm − 2.5 μm) and (i) R_{IR} (θ) (2.5 μm − 15 μm) across various AOI results in excellent hemispherical ε_{solar} and R_{IR}. (j) The SSAs' high absorptance ε_{solar} (θ) (0.3 μm − 2.5 μm) and (k) R_{IR} (θ) (2.5 μm − 15 μm) across different angles of polarization.

the W−SiO$_2$−W structure and the top Al$_2$O$_3$ anti-reflection layer and the detailed discussion can be found below Fig. S4. The solar irradiance is randomly distributed in a one-day cycle, and it is consequential to make the SSA facing to the sun all the time with the help of a dual-axis solar tracker system. The fabricated SSA has angular-independent hemispherical $\varepsilon_{solar}(\theta)$ > 0.90 (0.3 μm − 2.5 μm) (Fig. 1h) and $R_{IR}(\theta)$ > 0.93 (2.5 μm − 20 μm) (Fig. 1i (AOI, from 6° to 75°), and it enables the SSAs latitude-insensitive and to all day without solar-track systems for the non-concentrated solar thermal systems. Moreover, sunlight concentrates into beams with high energy density, and it is absorbed by solar absorbers in the concentrated solar thermal systems, while the incident angle of the concentrated beams is not always normal to the surface of solar absorbers. Therefore, the optical and thermal radiative properties at oblique angles of the solar absorber are vital for efficiently harvesting direct sunlight coming from various directions after an optical concentrator. In contrast, other SSAs report in literature often have directionally orientated structure, which enhances high ε_{solar}, (0°), but reduced ε_{solar}(>60°) [42,43]. As shown in Fig. 1h, for θ > 60°, the SSAs have a higher $\varepsilon_{solar}(\theta)$ than other SSAs. Besides, the hemispherical $\varepsilon_{solar}(\theta)$ > 0.89 (Fig. 1j; AOI, 6°) and

$R_{IR}(\theta)$ > 0.95 (Fig. 1k; AOI, 12°) for various polarization angles (from 6° to 75°), which makes it perfect to absorb lights of different angles of polarization. Here, Fig. 2 shows both the 3D contour plot of reflectivity spectra for the designed SSAs as functions of incident angle θ, and wavelength λ for transverse electric (TE), transverse magnetic (TM), and unpolarized waves. The simulated reflectivity remains low within visible and near-infrared region and high reflectivity (>0.95) in the mid-infrared region (3 μm − 15 μm) for unpolarized waves (Fig. 2c). Table S3 lists the reflectivity at 0.55 μm, which the irradiance peak of solar lies, incident light at various angles. For both TE and TM waves, the reflectivity of the designed absorber is low from 0° to 75°. However, the measured reflectivity of SSAs at 60° and 75° is higher than the simulated results, this is due to the fabrication process: the chemical bond (Si−O and Al−O) of SiO$_2$ and Al$_2$O$_3$ can be broken when collided with the charged energetic ions beams, resulting in the change of the atomic ratio of Si/O and Al/O. Note that, the reflectivity spectra show two dips around λ = 8.0 (or 7.8) μm and λ = 10.8 (or 10.5) μm (Fig. 2b and c), which are due to the surface phonon resonance of SiO$_2$ and Al$_2$O$_3$, respectively, and this is also confirmed by the specular reflectivity measurements (Fig. 2d-f). As shown in Supporting Fig. S5a-d, the
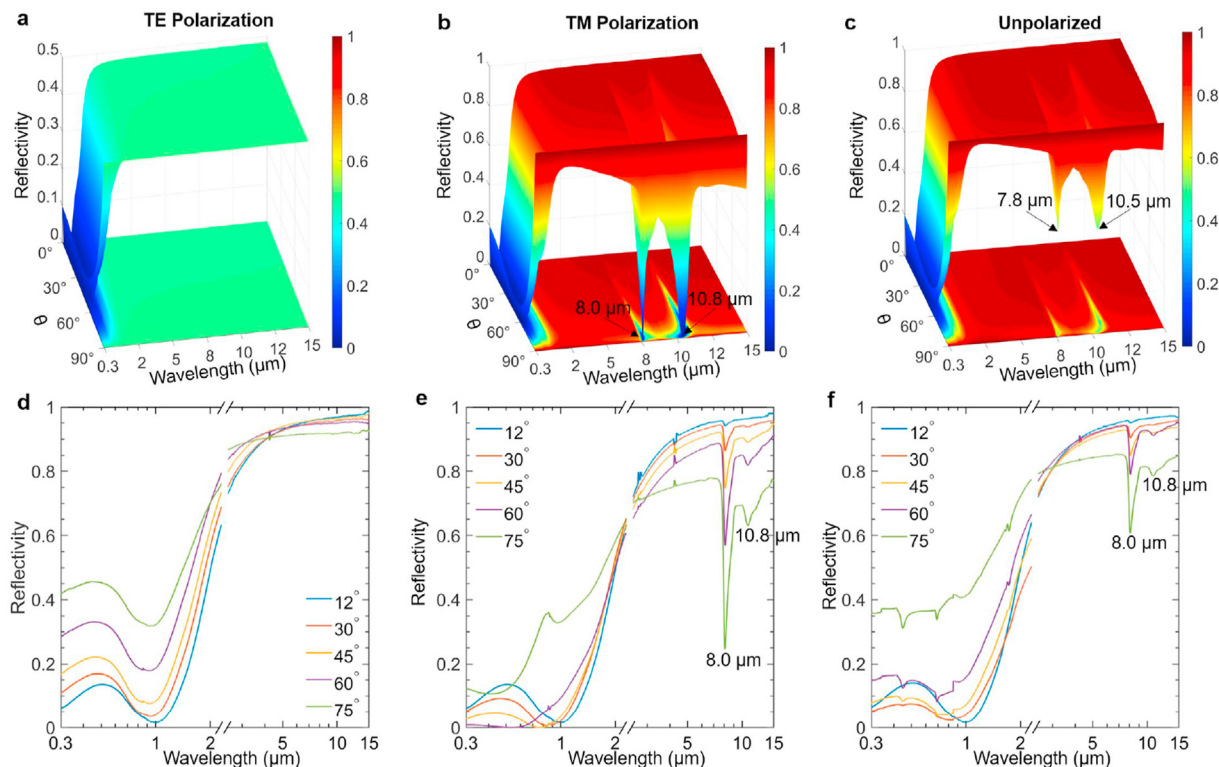
Fig. 2. Simulated angle-dependent TE-polarization (a), TM-polarization (b), and unpolarized (c) specular reflectivity spectra of SSAs' 3D plot and projected 2D contour plot as functions of wavelength and angle of incidence, θ. Measured specular reflectivity spectra of SSAs across angles at TE-polarization (d), TM-polarization (e), and unpolarized light (f).

removal of Al_2O_3 layer shows the vanish of the dip at 10.8 μm, and the removal of SiO_2 layer yields the disappearance of the dip at 8.0 μm. These two dips are in principle due to the sharp resonances of the extinction coefficient of Al_2O_3 and SiO_2 (Supporting Fig. S5f). Since both Al_2O_3 and SiO_2 are non-magnetic material, the permeability (μ) of Al_2O_3 and SiO_2 are considered to be 1, while it permittivity (ε, the square of the complex refractive indices: $n + i\kappa$) is a function of wavelength. From Supporting Fig S6 and Eqs. S1 and S2, we can see that how the polarized Fresnel reflection coefficients R^{TE} and R^{TM} are calculated as an example from permeability and permittivity, respectively. Therefore, the fluctuations of the permittivity contribute to the dips observed in the TM-polarization reflectivity spectra and the constant permeability produces no resonances in the TE-polarization reflectivity spectra. To conclude, the polarization dependence is induced by the sharp resonances of the extinction coefficients of Al_2O_3 and SiO_2. However, the irradiance intensity peak of 500 °C blackbody thermal radiation lies at 3.8 μm (Fig. 1a), while the blackbody emission power of 500 °C blackbody radiation at $\lambda = 8$ μm and $\lambda = 11$ μm only equals to 30% and 11% of the peak value. For higher temperature applications (>500 °C), the blue-shifts of blackbody radiation will make the proportion of thermal radiation at around $\lambda = 8$ μm and $\lambda = 11$ μm even smaller, and these dips are prominent only for higher incident angles; so it can be concluded that these two dips in reflectivity do not affect severely the selectivity performance of the SSAs. The overall absorptance of the fabricated samples at solar irradiance wavelength regime is 92%, while it shows a low emittance of 6.6% at a thermal wavelength with the measured spectral reflectivity under unconcentrated sunlight by solving Eqs. S4 and S5 (the integral interval of solar radiation is from 0.25 μm to 2.5 μm, and the integral interval of blackbody thermal radiation is in the range of 2.5 μm–15 μm).

3.3. Ambient thermal stability test and thermal degradation mechanism

To maintain high energy efficiency, the CSP system always works under the concentrated sunlight to obtain high operational temperature, so it is consequential to have a constant spectral performance for SSAs at high temperatures. For the sake of evaluating the radiative properties of SSAs after thermal annealing at elevated temperatures and long-time thermal stability tests, we measure the reflectivity spectra of the fabricated SSAs after each thermal test for 1-h thermal annealing (Fig. 3a) at a temperature from 25 °C to 500 °C and long-time thermal cycle at 400 °C (Fig. 3c), since we are aiming at the mid-temperature CSP applications (300 °C < T < 500 °C). Fig. 3b and d show the overall of ε_{solar}, R_{IR}, and η_{abs} of SSAs after elevated temperature and long-time thermal tests. The spectral reflectivity of the tested sample reduces from 25 °C to 200 °C (Fig. 3a and b), resulting in that the ε_{solar} decreases from 92.0% to 88.5% (95.3% remain) and thermal emittance, ε_{IR} increases from 6.6% to 12.53% (89.8% increase) and the η_{abs} reduces by 3.31%. Though the SEM topography of SSAs shows little change, the dielectric functions of SiO_2 and Al_2O_3 might change at elevated temperatures. The ε_{solar} and ε_{IR} keep changing from 200 °C to 500 °C, which results in a decrease in η_{abs} from 75.7% to 74.5%. This is possibly caused by the SSAs' topography damage, as shown in Fig. 3e for 400 °C and 500 °C.

Fig. 3c elucidates the reflectivity spectra of the fabricated samples after long-time thermal stability tests. The reflectivity spectra of SSAs changes severely after 400 °C thermal stability test over 12 h and ε_{solar} decreases from 92.0% to 85.2% (92.6% remain) and thermal emittance ε_{IR} increases from 6.6% to 12.5% (89.8% increase) and η_{abs} reduces by 3.39%. After that, from 12 h to 48 h, ε_{solar} and ε_{IR} barely change (Fig.3d). However, ε_{IR} increases from 48 h to 72 h and causes a drop of η_{abs}.
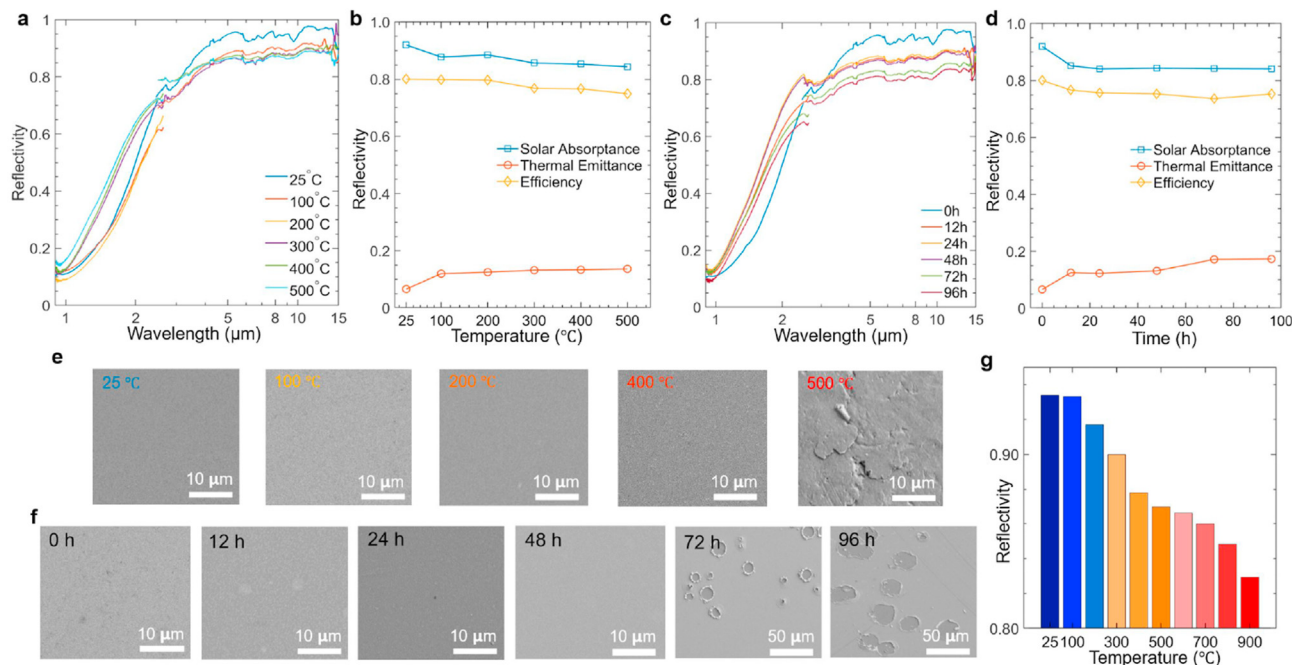
Fig. 3. Reflectivity spectra (a) and overall ε_{solar}, ε_{IR}, and η_{abs} (b) of the SSAs measured by FTIR spectrometer after 1-h thermal treatment at different temperatures under ambient environment. Reflectivity spectra (c) and overall ε_{solar}, ε_{IR}, and η_{abs} (d) of the SSAs at 400 °C after long-time thermal treatment. SEM topographic image of the fabricated SSAs sample as fabricated and after 1-h thermal annealing at various temperatures (e) and long-time thermal treatment (f). (The blackbody temperature is fixed to be 100 °C when calculate the η_{abs}) (g) Real-time measurement of R_{IR} for SSAs at elevated temperature under high vacuum ($<10^{-3}$Pa).

SEM topography images are employed to understand the mechanism that causes the degradation above 400 °C and after 72 h thermal treatment. Fig.3e shows the SEM topographic images of the SSAs surface before and after thermal annealing for 1 h. From 25 °C to 400 °C, it is difficult to see any apparent changes. When the temperature keeps going up from 400 °C to 500 °C, small cracks show up, which is also demonstrated in the reflectivity spectra in Fig. 3a, due to the thermal stress coming from the difference in thermal expansion coefficient between SiO$_2$ (0.55×10^{-6} m/m·K) and W (4.2×10^{-6} m/m·K) [24]. Fig. 3f shows the SEM topographic images of the SSAs surface before and after long-time thermal treatment. Little topographic change of SSAs can be seen from 12 h to 48 h, while small round cracks like burst bubbles appear after 72 h and become bigger after 96 h. It agrees well with the reflectivity spectra change of Fig. 3c. It provides a guideline for improvement approaching perfect SSAs by the utilization of other materials with a similar thermal expansion coefficient to avoid the thermal stress at high temperature and long-time annealing.

Fig. 3g shows that the R_{IR} of SSAs gradually drops heating under elevated temperatures. Each stepped drops from 100 °C to 400 °C is larger than that from 400 °C to 800 °C. It proves that most of the thermal stress between different layers of SSAs is released when heated from 100 °C to 400 °C. Combined with the SEM topographic image of Fig.3e, we conclude that the formation of cracks contributes more than the development of cracks to a decrease of R_{IR}. Even heated up to 900 °C, the R_{IR} of SSAs still remain 90.15% compared with the value at ambient temperature, this indicates that the combinations of SiO$_2$ and Al$_2$O$_3$ has the potential applications under high-temperature solar thermal systems.

3.4. Solar conversion efficiency investigations of fabricated multilayer SSAs

As discussed above, the designed structure of SSAs is demonstrated to be angular-insensitive, as well as thermal stable up to

400 °C. We employ the reflectivity measured by the UV/VIS/NIR spectrophotometer and FTIR spectrometer at room temperature (25 °C), as shown in Fig. 1g. The $\alpha_{\lambda,abs}$' and $\varepsilon_{\lambda,abs}$' are assumed to be independent of temperature as observed in Fig. 3a. The spectral integration for $\alpha_{\lambda,abs}$' and $\varepsilon_{\lambda,abs}$' is performed over wavelengths from 0.3 μm to 16 μm, which covers 99.9% of the solar radiation and only 4.7% of thermal radiation energy outside this spectral region for a 400 °C blackbody. The reflectivity of the ideal absorber is zero below the cutoff wavelength, while its reflectivity is unity beyond the cut-off wavelength to minimize thermal leakage from blackbody radiation (Fig. 1a, the dark-orange dot-dash line). The cut-off wavelength is optimized according to the shifts of blackbody thermal radiation at different operational temperatures to maximize the energy conversion efficiency, which defines an upper limit of system efficiency. The reflectivity of black surface, $R_{abs,black}$, is zero over the entire wavelength region and shows no spectral selectivity (Fig. 1a, the black long dash line).

The conversion efficiencies (Supplementary Note section 2) of SSAs are 84.28% and 86.32% for the simulated and measured spectral reflectivity at $T_{abs} = 100$ °C, respectively (Fig. 4a). The efficiency drops gradually to zero at the stagnation temperature of 396 °C and 486 °C using simulated and measured optical properties, respectively. The absorbed solar energy equals the blackbody re-emission energy (i.e., no solar thermal energy is harvested) at this point. The stagnation temperature of SSAs using the simulated reflectivity spectrum is higher than the one using the measured reflectivity spectrum since the reflectivity curve of the simulated one is steeper than the measured one over the transition wavelength region. The efficiency curves of SSAs with measured and simulated radiative properties intersect at 210 °C. The fabricated SSA has a higher efficiency than the designed SSA below 210 °C because the measured spectrum has a higher reflectivity than the simulated one from 7.7 μm to 20 μm, (as marked by red solid pentagram in Fig.1g). Half of the blackbody thermal radiation spreads in this wavelength region (the thermal radiation of a 210 °C
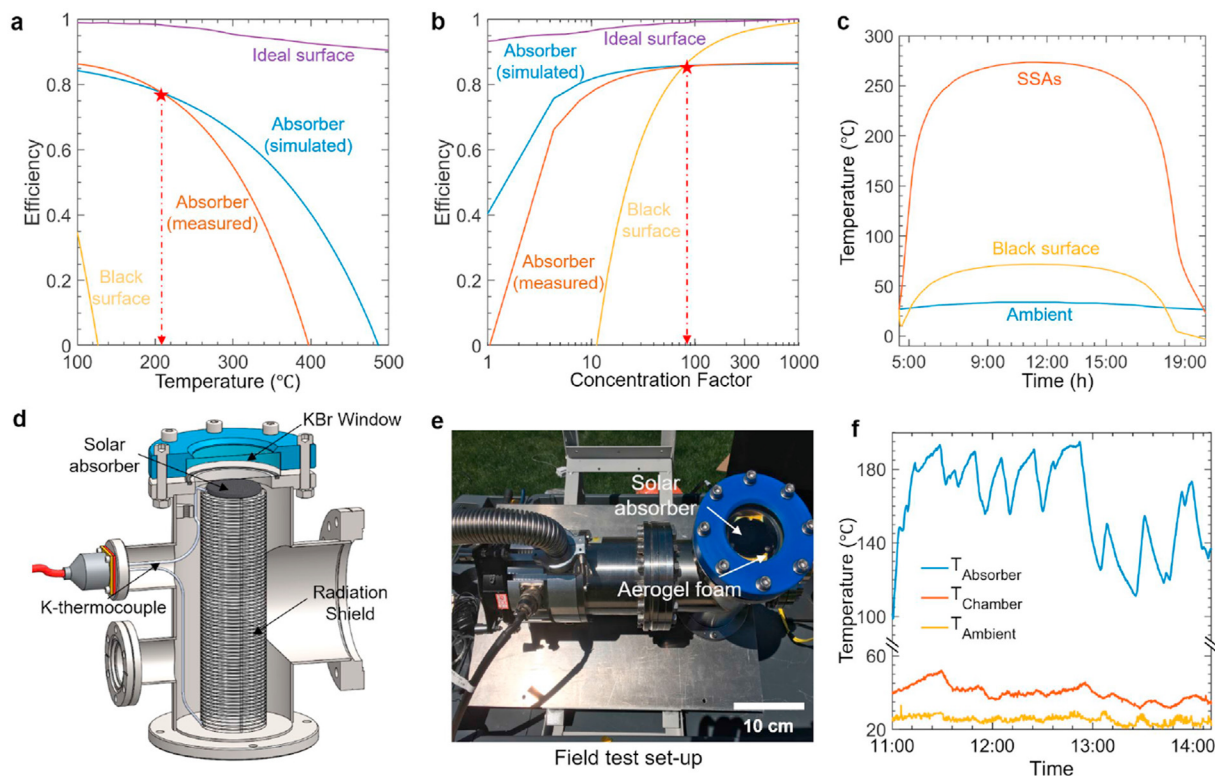
Fig. 4. (a) Solar to heat conversion efficiency as a function of absorber operational temperature, T_{abs}, for an ideal selective absorber, SSAs with reflectivity spectra of the measured or simulated, and a black surface, under the unconcentrated solar light (1 sun); (b) Solar to heat conversion efficiency for abovementioned four surfaces as a function of *CF*, at the operational temperature of $T_{abs} = 400\,°C$. (c) Thermal performance of the selective absorber (orange curve) and the black surface (yellow curve) over a one-day solar cycle from sunrise (5:00 a.m.) to 1 h after sunset (8:00 p.m.) at varying ambient temperature (blue curve) under 1 sun. Three-dimensional schematic (d) of the real (e) outdoor experimental setup. (f) The temperature variations of the sample's surface, vacuum chamber, and outdoor ambient environment.

blackbody spans from 3.0 μm to 15 μm). When the temperature goes above 210 °C, the efficiency of SSAs using simulated reflectivity spectrum exhibits an advantage than the measured one since the blackbody radiation blue-shifts to the shorter wavelength, where the simulated spectrum has a higher reflectivity than the measured. As a reference, the black surface can only convert 34.8% solar energy to heat at $T_{abs} = 100\,°C$, and its efficiency goes down to zero at 126 °C, which further demonstrates the significance of spectral selectivity in enhancing the solar to heat conversion efficiency. On the other hand, the efficiency of the multilayered absorber is 17% and 20% lower than the ideal surface at $T_{abs} = 100\,°C$ with measured optical properties and simulated radiative spectrum data, respectively. This gap becomes large when the stagnation temperature increases. It mainly results from the larger thermal emittance (around 0.09) in the mid-infrared regime and the cut-off wavelength of the ideal surface is optimized at each temperature according to Wien's displacement law, while the cutoff wavelength of selective absorber keeps unchanged at around 1.2 μm. Simultaneously, the reflectivity spectrum of the ideal surface changes much sharply at the cut-off point than the multilayered SSAs, comparing Fig. 1a and g. Therefore, the geometry parameters of the multilayered SSAs need to be optimized to make the cutoff wavelength perfectly matched the operational temperature.

Fig. 4b shows the efficiency as a function of *CF*, from 1 to 1,000, when $T_{abs} = 400\,°C$, aiming at a mid-temperature application. The cutoff wavelength of the ideal surface is optimized according to different *CF*. This indicates an upper limit for the SSAs' performance under different *CF*. The energy efficiency of SSAs with measured or simulated optical properties and the black surface keeps going up with the increasing of *CF*. The efficiency of SSAs with the measured

reflectivity spectrum is lower than the simulated one because the simulated spectrum has a higher solar absorptance than the measured one. For the black surface, its energy conversion efficiency becomes greater than zero at around 12 suns and climbs close to the ideal surface when the *CF* = 1000 since the solar radiation heat flux is much larger than the 400 °C blackbody thermal radiation under 1000 suns.

3.5. Thermal performance investigations under unconcentrated solar radiation

Fig. 4c shows the calculated transient temperature variations of SSAs and the black surface under one sun over a solar cycle in Boston, Massachusetts [44] using the ambient temperature [44] and the solar illumination data [45] of July 10, 2018 (Supplementary Note section 3). The highest temperature of the SSAs is 273 °C, while the highest temperature of the black surface is 72 °C. The thermal performance of the SSA is overwhelmingly better than the black surface at any time under sunshine. The highest temperature difference between SSAs and the black surface is 311 °C under 20 suns (Supporting Fig. S7), which is higher than the temperature difference under one sun (201 °C). We evaluate the outdoor test performance by measuring the stagnation temperature under unconcentrated solar radiation in Kingston, Rhode Island on May 27, 2019. A SSAs sample was placed in a 100 cm diameter vacuum chamber which was equipped with a Potassium bromide (KBr) window (70 cm in diameter) (Fig. 4d and e). The KBr window is highly transparent (>93%) from UV to the mid-infrared range, which allows sunlight to come in and the thermal radiation of the heated SSAs re-emit to the sky. The vacuum chamber was set on a
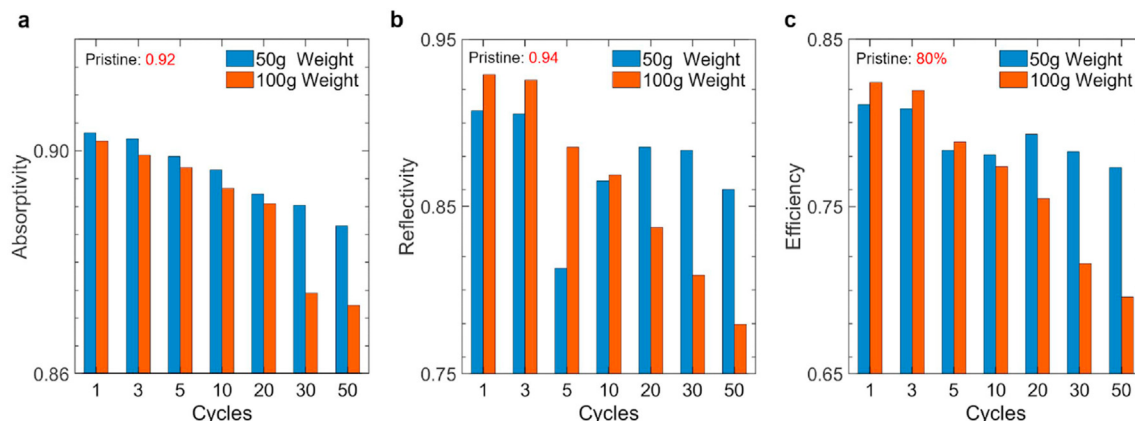
Fig. 5. ε_{solar} (a), R_{IR} (b), and η_{abs} (c) after the different abrasion tests under different weight (50 g/100 g) as a function of cycles.

mounting frame with an angle of ~ 32° to ensure the absorber was normal to the incoming sunlight. A K-type thermocouple was secured to the back of the SSAs sample with Kapton tape. Another K-type couple was taped to the bottom of the radiation shield to measure the local temperature of the vacuum chamber. To eliminate the conductive and radiative heat losses, we supported the absorber sample with low thermal conductivity (29 mW/m·K) aerogel tiles that were on top of the radiation shield made of several double-side polished aluminum sheets. The vacuum chamber was pumped continuously to be ~ 5 × 10^{-3} Pa with the turbomolecular pump to eliminate the convective and conductive thermal losses from the air. The warmed up to the maximum stagnation temperature of 193.5 °C at around 11:30 since the weather was partly cloudy (Fig. 4f), the temperature of the vacuum chamber and the absorber sample showed strong fluctuations during the test and was lower than the calculated maximum temperature. The stagnation temperature is enough for the rooftop solar thermal systems even under partly cloudy weather.

3.6. SSAs' surface abrasion robustness tests

The lifetime of the SSAs is not only shortened by a long-term exposure to high temperature, humidity, atmospheric pollution, but also sensitive to mechanical abrasion [46]. Thus, a spectrally selective surface that is robust to the mechanical abrasion is highly demanded in CSP systems. Fig. 5a-c show ε_{solar} (a), R_{IR} (b), and η_{abs} (c) of SSAs after each abrasion cycle (the definition of one abrasion cycle is in Supporting Fig. S3). It can be found that the ε_{solar}, R_{IR}, and η_{abs} remain 94.6%, 83.5%, and 86.9% after 50 abrasion cycles under 100 g weight. The R_{IR} of SSAs under 50 g weight first drops and then increases, since the pressure of 50 g weight can remove part of the top deposited SiO_2 and Al_2O_3 layer and make the bottom W layer exposed out in 5 cycles. While the 100 g weight can make part of the bottom W layer exposed out only in 1 cycle. Since the abrasion resistance tests will break the fabricated SSAs layer, the ε_{solar} keeps decreasing whichever 50 g or 100 g weight is placed above. The η_{abs} of 50 g weight tests first decreases and goes up after 10 cycles, due to the R_{IR} fluctuations of 50 g weight tests.

4. Conclusion

The spectral selectivity and thermal performance of multilayered SSAs consisting of Al_2O_3−W−SiO_2−W stacks are investigated analytically and experimentally. The FP resonance of W−SiO_2−W stacks enables a high broadband solar absorptance and the top Al_2O_3 anti-reflection layer reinforces its performance. This

structure demonstrates 92% solar absorptance and 6% thermal emittance (100 °C blackbody) the blackbody thermal radiation region. Oblique reflectivity is also experimentally characterized to show high spectral selectivity for both TE- and TM-polarizations, which demonstrates its angular and polarization insensitivity. High-temperature thermal annealing performed at elevated temperatures for 1 h shows the fabricated SSAs maintain its wavelength selectivity at even 400 °C and 500 °C. The high-temperature thermal stability test is investigated under 400 °C for 12 h, 24 h, 48 h, 72 h, and 96 h cycles, and it demonstrates SSAs keep good selectivity within 48 h, while slight degradation of spectral selectivity happens after the 72 h and 96 h thermal treatment. Real-time reflectivity measurements show that the material displays only a minor change in optical properties above 800 °C. Our study indicates that the proposed metamaterial exhibits thermal stability and practically retains its optical proprieties even after 96 h operation at 400 °C. Retention of optical properties after high-temperature annealing can be attributed to the pattern-free design of the material as cracks can be significantly more detrimental to the optical properties of surface designs such as gratings. The outdoor tests show a peak stagnation temperature of 193.5 °C, and thus indicate its tremendous potential for low temperature solar thermal applications in the absence of a solar concentrator. Additionally, the surface abrasion test yields that SSAs have a robust resistance to sandpaper abrasion attack for a long-duration practical application. Abrasion resistance can also be attributed to this pattern-free design.

Credit author statement

Declaration of competing interest

The authors declare that they have no known competing financial interests or personal relationships that could have appeared to influence the work reported in this paper.

Acknowledgments

Appendix A. Supplementary data

Supplementary data to this article can be found online at https://doi.org/10.1016/j.mtener.2021.100725.

References

[1] D. Abbott, Keeping the energy debate clean: how do we supply the world's energy needs? Proc. IEEE 98 (2010) 42–66.

[2] A. Polman, H.A. Atwater, Photonic design principles for ultrahigh-efficiency photovoltaics, Nat. Mater. 11 (2012) 174–177.

[3] T.M. Tritt, H. Böttner, L. Chen, Thermoelectrics: direct solar thermal energy conversion, MRS Bull. 33 (2008) 366–368.

[4] D. Gust, T.A. Moore, A.L. Moore, Solar fuels via artificial photosynthesis, Acc. Chem. Res. 42 (2009) 1890–1898.

[5] D. Mills, Advances in solar thermal electricity technology, Sol. Energy 76 (2004) 19–31.

[6] D. Kraemer, B. Poudel, H.-P. Feng, J.C. Caylor, B. Yu, X. Yan, Y. Ma, X. Wang, D. Wang, A. Muto, et al., High-performance flat-panel solar thermoelectric generators with high thermal concentration, Nat. Mater. 10 (2011) 532–538.

[7] N. Wang, L. Han, H. He, N.-H. Park, K. Koumoto, A novel high-performance photovoltaic–thermoelectric hybrid device, Energy Environ. Sci. 4 (2011) 3676–3679.

[8] R. Kaempener, Solar Heat for Industrial Processes, IEA-ETSAP and IRENA Technology Brief, 2015, p. E21.

[9] X. Lim, How heat from the sun can keep us all cool, Nature News 542 (2017) 23.

[10] H.C. Barshilia, S. John, V. Mahajan, Nanometric multi-scale rough, transparent and anti-reflective zno superhydrophobic coatings on high temperature solar absorber surfaces, Sol. Energy Mater. Sol. Cells 107 (2012) 219–224.

[11] H. Wang, I. Haechler, S. Kaur, J. Freedman, R. Prasher, Spectrally selective solar absorber stable up to 900c for 120 h under ambient conditions, Sol. Energy 174 (2018) 305–311.

[12] H. Wang, V.P. Sivan, A. Mitchell, G. Rosengarten, P. Phelan, L. Wang, Highly efficient selective metamaterial absorber for high-temperature solar thermal energy harvesting, Sol. Energy Mater. Sol. Cell. 137 (2015) 235–242.

[13] R. Siegel, Thermal Radiation Heat Transfer, Volume 1, CRC press, 2001.

[14] F. Cao, K. McEnaney, G. Chen, Z. Ren, A review of cermet-based spectrally selective solar absorbers, Energy Environ. Sci. 7 (2014) 1615–1627.

[15] Y. Zhao, C. Fu, Design of multiband selective near-perfect metamaterial absorbers with sio 2 cylinder/rectangle shell horizontally embedded in opaque silver substrate, Int. J. Heat Mass Tran. 113 (2017) 281–285.

[16] H. Kocer, S. Butun, Z. Li, K. Aydin, Reduced near-infrared absorption using ultra-thin lossy metals in fabry-perot cavities, Sci. Rep. 5 (2015) 1–6.

[17] A. Ghobadi, S.A. Dereshgi, H. Hajian, B. Bozok, B. Butun, E. Ozbay, Ultra-broadband, wide angle absorber utilizing metal insulator multilayers stack with a multi-thickness metal surface texture, Sci. Rep. 7 (2017) 1–10.

[18] Z. Yang, Y. Chen, Y. Zhou, Y. Wang, P. Dai, X. Zhu, H. Duan, Microscopic interference full-color printing using grayscale-patterned fabry–perot resonance cavities, Advanced Optical Materials 5 (2017) 1700029.

[19] A. Ghanekar, M. Sun, Z. Zhang, Y. Zheng, Optimal design of wavelength selective thermal emitter for thermophotovoltaic applications, J. Therm. Sci. Eng. Appl. 10 (2018), 011004.

[20] H. Wang, L. Wang, Perfect selective metamaterial solar absorbers, Opt Express 21 (2013) A1078–A1093.

[21] A. Ghanekar, Y. Tian, S. Zhang, Y. Cui, Y. Zheng, Mie-metamaterials-based thermal emitter for near-field thermophotovoltaic systems, Materials 10 (2017) 885.

[22] K. Chen, R. Adato, H. Altug, Dual-band perfect absorber for multispectral plasmon-enhanced infrared spectroscopy, ACS Nano 6 (2012) 7998.

[23] V. Stelmakh, V. Rinnerbauer, R. Geil, P. Aimone, J. Senkevich, J. Joannopoulos, M. Soljačić, I. Celanovic, High-temperature tantalum tungsten alloy photonic crystals: stability, optical properties, and fabrication, Appl. Phys. Lett. 103 (2013) 123903.

[24] M. Chirumamilla, A.S. Roberts, F. Ding, D. Wang, P.K. Kristensen, S.I. Bozhevolnyi, K. Pedersen, Multilayer tungsten-alumina-based broadband light absorbers for high-temperature applications, Opt. Mater. Express 6 (2016) 2704–2714.

[25] M. Langlais, H. Bru, P. Ben-Abdallah, et al., High temperature layered absorber for thermo-solar systems, J. Quant. Spectrosc. Radiat. Transf. 149 (2014) 8–15.

[26] V. Teixeira, E. Sousa, M. Costa, C. Nunes, L. Rosa, M. Carvalho, M. Collares-Pereira, E. Roman, J. Gago, Spectrally selective composite coatings of cr–cr2o3 and mo–al2o3 for solar energy applications, Thin Solid Films 392 (2001) 320–326.

[27] Q.-C. Zhang, D.R. Mills, New cermet film structures with much improved selectivity for solar thermal applications, Appl. Phys. Lett. 60 (1992) 545–547.

[28] D. Gogova, Optical and structural characterization of tungsten-based cvd metal oxide coatings, Mater. Lett. 30 (1997) 109–113.

[29] Q.-C. Zhang, Y. Shen, High performance w–aln cermet solar coatings designed by modelling calculations and deposited by dc magnetron sputtering, Sol. Energy Mater. Sol. Cell. 81 (2004) 25–37.

[30] T.S. Sathiaraj, R. Thangaraj, H. Al Sharbaty, M. Bhatnagar, O. Agnihotri, Ni-al2o3 selective cermet coatings for photothermal conversion up to 500 c, Thin Solid Films 190 (1990) 241–254.

[31] J. Wang, B. Wei, Q. Wei, D. Li, Optical property and thermal stability of mo/mo–sio2/sio2 solar-selective coating prepared by magnetron sputtering, Phys. Status Solidi 208 (2011) 664–667.

[32] H.C. Barshilia, P. Kumar, K. Rajam, A. Biswas, Structure and optical properties of ag–al2o3 nanocermet solar selective coatings prepared using unbalanced magnetron sputtering, Sol. Energy Mater. Sol. Cell. 95 (2011) 1707–1715.

[33] C. Nunes, V. Teixeira, M. Prates, N. Barradas, A. Sequeira, Graded selective coatings based on chromium and titanium oxynitride, Thin Solid Films 442 (2003) 173–178.

[34] A. Ghanekar, L. Lin, Y. Zheng, Novel and efficient mie-metamaterial thermal emitter for thermophotovoltaic systems, Opt Express 24 (2016) A868–A877.

[35] H. Wang, H. Alshehri, H. Su, L. Wang, Design, fabrication and optical characterizations of large-area lithography-free ultrathin multilayer selective solar coatings with excellent thermal stability in air, Sol. Energy Mater. Sol. Cell. 174 (2018) 445–452.

[36] A. Al-Rjoub, L. Rebouta, N. Cunha, F. Fernandes, N. Barradas, E. Alves, W/alsitinx/sialtioynx/sialox multilayered solar thermal selective absorber coating, Sol. Energy 207 (2020) 192–198.

[37] S. Han, J.-H. Shin, P.-H. Jung, H. Lee, B.J. Lee, Broadband solar thermal absorber based on optical metamaterials for high-temperature applications, Advanced Optical Materials 4 (2016) 1265–1273.

[38] P.J. Call, Proceedings: Second Annual Conference on Absorber Surfaces for Solar Receivers, January 24 & 25, 1979, Technical Report, National Renewable Energy Lab.(NREL), Golden, CO (United States), 1979.

[39] Almeco group, TiNOX, 2020. https://www.wunderground.com/history/daily/us/ma/boston/KBOS/date/2018-7-10.

[40] Solec Solkote. https://www.pveducation.org/pvcdrom/properties-of-sunlight/calculation-of-solar-insolation, 2020.

[41] Y. Tian, A. Ghanekar, L. Qian, M. Ricci, X. Liu, G. Xiao, O. Gregory, Y. Zheng, Near-infrared optics of nanoparticles embedded silica thin films, Opt Express 27 (2019) A148–A157.

[42] G. Pettit, J. Cuomo, T. DiStefano, J. Woodall, Solar absorbing surfaces of anodized dendritic tungsten, IBM J. Res. Dev. 22 (1978) 372–377.

[43] J. Zhu, Z. Yu, G.F. Burkhard, C.-M. Hsu, S.T. Connor, Y. Xu, Q. Wang, M. McGehee, S. Fan, Y. Cui, Optical absorption enhancement in amorphous silicon nanowire and nanocone arrays, Nano Lett. 9 (2009) 279–282.

[44] Weatherground, Weather Conditions, 2018. Online, https://www.wunderground.com/history/daily/us/ma/boston/KBOS/date/2018-7-10. (Accessed 10 July 2018). accessed.

[45] Pveducation.ORG, Calculation of Solar Insolation, 2018. https://www.pveducation.org/pvcdrom/properties-of-sunlight/calculation-of-solar-insolation.

[46] C.E. Kennedy, Review of Mid-to High-Temperature Solar Selective Absorber Materials, Technical Report, National Renewable Energy Lab., Golden, CO.(US), 2002.